Processes and patterns of flow, erosion, and deposition at shipwreck sites: a computational fluid dynamic simulation

R. Quinn[1] and T.A.G. Smyth[2]

[1] School of Geography and Environmental Sciences, Ulster University, Coleraine BT52 1SA, Northern Ireland, RJ.Quinn@ulster.ac.uk (author for correspondence)

[2] Department of Geography and Environmental Science, Liverpool Hope University, Hope Park, Liverpool, L16 9JD, United Kingdom.

Keywords

Computational fluid dynamics; shipwreck; fluid flow; site formation processes; hydrodynamics; scour; deposition

Abstract

Shipwreck sites are open systems, allowing the exchange of material and energy across system boundaries. Physical processes dominate site formation at fully submerged wreck sites, and in turn influence chemical and biological processes at many stages of site formation. Scouring presents a fundamental yet poorly understood threat to wreck sites, and the processes and patterns of erosion and deposition of sediments and artefacts at wreck sites are poorly understood. Laboratory and field based experiments to study these phenomena are time-consuming and expensive. In this study open-source computational fluid dynamic (CFD) simulations are used to model the processes and patterns of flow, erosion, and deposition at fully submerged wreck sites. Simulations successfully capture changes in the flow regime in the environment of the wreck as a function of incidence angle, including flow contraction, the generation of horseshoe vortices in front of the wreck, the formation of lee-wake vortices behind the structure, and increased turbulence and shear stress in the lee of the wreck site. CFD simulations demonstrate that horseshoe vortices control scour on the upstream face of structure, but play a minimal role in scouring on the lee side. Lee-wake vortices dominate behind the structure, with low pressure zones in the lee of the wreck capturing flow. The amplification and reduction of wall shear stress and turbulent kinetic energy in the lee of the vessel form distinctive patterns in relation to flow direction, with areas of amplified and reduced wall shear stress and turbulent kinetic energy demonstrating excellent spatial correlation with erosional and depositional patterns developed at real-world wreck sites.

1. Introduction

Erosional and depositional features form in the lee of obstacles on the seafloor and are widely reported from all offshore environments (Whitehouse, 1998). Natural features such as rock outcrops and anthropogenic obstacles including breakwaters, pilings, foundations, and shipwrecks give rise to sediment deposits and scour features in their wake (Astley et al., 2014; Whitehouse et al., 2010). An understanding of the processes that form and maintain these erosional and depositional features is critical as they can control the stability and long-term integrity of submerged anthropogenic structures.

In archaeological investigations, scouring is reported widely, from nearshore submerged wreck sites in shallow water (Arnold et al. 1999; Baeye et al., 2016; Caston 1979; McNinch et al. 2001; Quinn et al. 1997; Wheeler 2002) to deep-water sites on the continental shelf and beyond (Ballard et al. 2000, 2002; McCann and Oleson 2004; Uchupi et al. 1988). Scour is reported from intact and scattered wreck sites (Arnold et al. 1999; Caston 1979; McNinch et al. 2001; Quinn 2006; Wheeler 2002) and from individual artifacts and artifact scatters (Ballard et al. 2000, 2002; McCann and Oleson 2004). In maritime archaeology the focus on site formation theory (Muckelroy 1978; O'Shea 2002; Quinn 2006; Stewart 1999; Ward et al. 1999) and a general acceptance that physical processes dominate site formation in the early stages (Ward et al. 1999) suggest that a greater understanding of scouring and associated depositional and erosional processes and patterns at wreck sites is important.

The aim of this study is to investigate the mechanisms responsible for the formation and evolution of scour and depositional features under secondary flows using computational fluid dynamic (CFD) simulations (Smyth and Quinn, 2014). Until now, we have only been able to investigate patterns of erosion and deposition through field-based investigations (Caston, 1979; Astley et al., 2014) or laboratory based physical models (Saunders, 2005; Testik et al., 2005), while the complex processes giving rise to the patterns have been difficult, time-consuming and expensive to investigate. CFD allows us to examine these processes in detail. The results represent a significant breakthrough in understanding fluid flow and erosional and depositional processes and patterns at submerged wreck sites.

2. Theory: patterns of erosion and deposition at wreck sites

Scouring is associated with areas of elevated shear stress, where shear stress exerted by moving water is proportional to the square of the flow velocity. In the ocean, the majority of erosion, deposition, and transport of sediment takes place in the boundary layer adjacent to

the seafloor. The extent to which sediment movement takes place depends on the amount of turbulence (turbulent kinetic energy, TKE) and shear stress (wall shear stress, WSS) exerted on the bed. Sediment moves on the seafloor when the shear stress at the bed exceeds the frictional and gravitational forces holding the grains to the bed (i.e. when critical shear stress is reached). Marine scour occurs when sediment is eroded by oscillatory flows such as waves, by directional flows (tidal, river, or density induced), or a combination of both (Whitehouse 1998). The introduction of an object (shipwreck or engineering structure) to the seafloor may initiate scour (Soulsby 1997; Whitehouse 1998; Quinn 2006), and scour processes can ultimately lead to complete failure and collapse of the structure (Soulsby 1997; Whitehouse 1998). Scour signatures are widely reported from the marine environment, and their development and importance in short- and long- term site evolution are noted in shipwreck archaeology (Arnold et al. 1999; Baeye et al., 2016; Caston 1979; McNinch et al. 2001; Quinn 2006; Trembanis and McNinch 2003; Uchupi et al. 1988; Ward et al. 1999).

In summary, the introduction of an object to the seafloor leads to an increase in flow velocity (due to continuity) and turbulence (due to the generation of vortices; Whitehouse 1998). Scouring subsequently results in the lowering of the seabed due to flow velocity increase near the object, a resulting increase in the *local* Shields parameter (a non-dimensional number used to calculate the initiation of motion of sediment in a fluid flow), and subsequent divergences in the sediment transport regime (Voropayev et al. 2003). Therefore the introduction of an object to the seafloor causes changes in the flow regime in its immediate environs, resulting in one, or a combination of, the following: flow contraction; the formation of a horseshoe vortex in front of the structure; the formation of lee-wake vortices behind the structure (sometimes accompanied by vortex shedding); turbulence; the occurrence of reflection and diffraction waves; wave breaking; and sediment liquefaction promoting material loss from the site (Sumer et al. 2001). These processes increase local sediment transport and subsequently lead to scour (Sumer et al. 2001).

The flow around a shipwreck is three-dimensional and consists of two basic structures (Testik et al. 2005; Quinn, 2006): the horseshoe vortex formed at the front of the structure and the lee-wake vortex formed behind. The horseshoe vortex is created by the rotation of the incoming flow, and under the influence of the adverse pressure gradient produced by the structure, rolls up to form a swirling vortex around the structure, and trails off down-flow (Sumer et al. 1997). Vortex shedding sometimes occurs, where self-propelling, closed ring structures are formed and transported by the flow (Testik et al. 2005). Lee wake vortices are formed by the rotation in the boundary layer over the surface of the object. End effects

from the bow and stern of the vessel play a dominant role in the flow pattern and strongly modify the structure of vortices (Testik et al. 2005; Quinn, 2006). Lee wake vortices emanating from the surface of the object are brought together in the vicinity of the structure due to flow convergence (Hatton et al. 2004; Smith et al. 2004; Testik et al. 2005). Additionally, two counter-rotating vortices form a vortical region in the near wake on the lee side of the object (Testik et al. 2005).

When scour occurs on fine-grained (silt or clay) seabeds, the eroded material is carried away from the wreck site in suspension (Baeye et al., 2016), leaving a seafloor depression that may not readily be in-filled by natural processes (Whitehouse et al. 2011). When scour occurs in coarse-grained deposits (sand or gravel), it usually results in local deposition of the eroded material. As the majority of wrecks of archaeological interest are located in shelf seas dominated by sand- and/or gravel-substrates, this study focuses on sites located in coarse-grained deposits only.

Caston (1979), Saunders (2005), Quinn (2006), and Quinn et al. (2016) previously illustrated complex patterns in the formation of scour and depositional features at wrecks sites, and noted the size and morphology of scour features are sensitive to the orientation of the obstacle relative to flow. Knowledge of these patterns and inferred processes have been largely derived from field observation through remote sensing (Caston, 1979; Quinn, 2006) and laboratory-based physical models (Saunders, 2005; Testik et al., 2005). However, the characteristics of the flows that develop behind shipwrecks, the stresses and turbulences that are induced by the obstacle, and their relationship with the angle of incidence of the flow remain poorly understood.

In engineering, scour is broadly classified as local scour (e.g. steep-sided scour pits at individual obstructions), global or dishpan scour (shallow broad depressions developed around installations), or general seabed movement, resulting in erosion, deposition or bedform development (Whitehouse 1998). In this study, the terms local scour (steep-sided scour pits formed in the immediate area of the wreck) and wake scour (shallower elongate extended linear depressions formed parallel to peak flow) are adopted following Saunders (2005).

3. Material and methods

3.1 Experimental setup

CFD simulations were conducted using a 'generic' hull shape (Figure 1) to represent the shipwreck. The hull of *Jylland* (launched 1860), one of the world's largest wooden warships (designed as both a screw-propelled steam frigate and a sail ship), was modelled in *SketchUp* and converted to a stereolithography (STL) file. SnappyHexMesh, the native mesh generator of the CFD software package OpenFOAM®, was used to produce the final three-dimensional computational domain. The hull was positioned in the centre of a 500 x 500 x 40 m domain which increased in resolution from 25 m at the boundaries to 0.125 m at the wreck site, finer than the resolution used by Smyth and Quinn (2014) at which mesh independence was achieved. The bottom 2 m of the hull was placed beneath the seabed, leaving 5 m of the structure exposed. The seabed was prescribed a roughness length (z_0) of 0.06 m, the equivalent of rippled sand (Johns, 1983), while the water surface was defined to produce zero gradient with the flow. This model was designed to mimic a typical fully submerged wreck site in a shelf sea environment, and the domain size and resolution was designed to optimize model run times while capturing near-field and far-field erosional and depositional signatures.

3.2 Approaching flow

The secondary flows that develop in the presence of a shipwreck are formed by modification of the approaching flow. Flow can be described using the Navier-Stokes equations; however, calculation of the complete equations in fully turbulent flow is computationally prohibitive. In these simulations flow was modelled using the Reynolds-averaged Navier-Stokes (RANS) equations using OpenFOAM®. The RANS equations decompose fluid movement into time-averaged and fluctuating quantities, providing an approximate solution of the Navier-Stokes equations.

TKE and turbulence dissipation rate (ε) was calculated using renormalization group theory (RNG). This method was employed due to the excellent comparison between measured and modelled data in a wind tunnel over a backward facing step (Yakhot et al., 1992) and in field experiments over three-dimensional natural complex landforms (Smyth et al., 2013; Hesp et al., 2015).

As flow in the lee of a shipwreck is intrinsically unsteady, the large time-step transient solver for incompressible flow (PIMPLE) was used. Simulations were considered complete once the initial solver residuals representing the absolute error of a variable were 5 orders of magnitude smaller than the maximum calculated. To represent determinative flow conditions, 100 time steps of each simulation were averaged from which flowlines (the path

traced by a massless particle), velocity, turbulent kinetic energy, wall shear stress and pressure were visualized.

Fluid flow at the inlet of the computational domain was defined as a steady logarithmic boundary layer equal to 1.30 m s^{-1} 2 m above the seabed. Simulations were conducted at 15° increments, from perpendicular (90°) to parallel to flow (0°); a total of 7 simulations. To represent water at 10°C, the fluid was prescribed a kinematic viscosity of 1.307 m^2 s^{-1}.

4. Results

4.1 General hydrodynamic environment in the lee of the hull

The general hydrodynamic environment in the lee of the submerged hull structure is illustrated in a series of 3-dimensional CFD visualizations (Figure 2). Horizontal flow separation occurs in the formation of two opposing vortices in the lee of the wreck (Figure 2a), with low-velocity zones developing on the upstream and downstream side of the hull structure, and high velocity zones developing in the water column above the wreck and on the seabed at the bow and stern of the vessel (Figure 2a). A high-pressure zone is induced on the upstream side of the hull and a low pressure zone formed on the downstream side (Figure 2b). Patterns of turbulence in the water column and on the seafloor (Figure 2c) largely mirror the patterns in velocity, with a zone of high turbulence developed in the water column on the downstream side of the hull and zones of elevated turbulence developed on the seafloor on the upstream side of the wreck and at the bow and stern (Figure 2c).

The flow velocity and patterns of pressure (P), WSS, and TKE are now discussed as a function of incidence at increments of 15°; from the hull orientated perpendicular to flow (at 90°) to parallel to flow (at 0°) (Figures 3-9; Table 1).

4.2 Hull at 90° to flow

Figure 3 shows typical CFD simulations for the submerged hull at an incident angle of 90° under a uni-directional flow of velocity 1.3 m s^{-1}. At this angle of incidence, flow and stress patterns are almost symmetrical around a flow-parallel plane of symmetry through the centre of the hull. On encountering the hull, an adverse pressure gradient induces small clockwise horseshoe vortices at the near-vertical wall, and the approaching flow is diverted over and around the structure, increasing in velocity (Figures 3b and 3c). Flow contraction occurs at the bow and stern. Horizontal flow separation takes place, with a counter rotating

low-velocity vortex pair developing in the low-pressure zone downstream of the hull (Figures 3a to 3c). Overall, the flow velocity structure is complex (Figure 3c), but virtually symmetrical around the plane. Low velocity zones form immediately upstream and downstream of the hull. Two crescentic regions of increased velocity originate from the bow and stern, converging downstream. A central high-velocity, flow-parallel zone is located between the two counter-rotating vortices (Figure 3c). A high-pressure zone develops upstream, probably by pressure-induced down-flow on the seafloor (Figure 3d). Immediately in the lee of the hull, a low pressure zone develops and extends downstream for approximately one full length. This is in turn replaced by a zone of intermediate pressure (Figure 3d). Two crescentic regions of amplified wall shear stress (WSS, Figure 3e) and turbulent kinetic energy (TKE, Figure 3f) originate at the bow and stern, coincident with the zones of elevated flow velocity modelled in the CFD simulations (Figure 3c). Furthermore, in the TKE simulation, two symmetrical turbulent zones form parallel to dominant flow, emanating approximately one ship-length from the hull. Zones of low WSS and low TKE form immediately in the lee of the hull and on the upstream side of the structure.

4.3 Hull at 75° to flow

As the approaching flow becomes more acute, the patterns developed in the CFD simulation become increasingly asymmetrical. Figure 4 shows typical CFD simulations for the submerged hull at an incident angle of 75° under a uni-directional flow of velocity 1.3 m s^{-1}. At this angle, flow contraction, flow separation and the development of the horseshoe vortex on the upstream side of the hull structure are observed (Figures 4a and 4b). Counter-rotating low-velocity vortices are again developed in the lee of the hull, with the in-flow vortex dominant. The low-velocity (Figure 4c) and low-pressure (Figure 4d) zones developed downstream are skewed along a line parallel to the flow, with greater flow-contraction and higher velocities recorded at the bow than the stern (Figures 4b and 4c). WSS and TKE patterns broadly correlate (Figures 4e and 4f) with zones of high shear stress and turbulence extending from the bow and stern, with higher values recorded at and in the lee of the bow section. Additionally, two asymmetric turbulent zones form downstream of the hull, separated and surrounded by zones of low turbulence, elongated parallel to the flow direction (Figure 4f).

4.4 Hull at 60° to flow

Figure 5 shows typical CFD simulations for the submerged hull at an incident angle of 60° under a uni-directional flow of velocity 1.3 m s^{-1}. At 60°, the upstream vortex developed at

the bow almost completely dominates vortex development in the lee of the structure. A small downstream vortex is developed in the lee of the stern, but it is much smaller in terms of magnitude and space (Figures 5a and 5b). Flow contraction and downward pressure is greater at the bow (Figures 5a to 5d), with the low pressure zone developed in the lee of the vessel skewed in direction of flow. Again, the WSS and TKE plots correlate (Figures 5e and 5f) with high shear stress and turbulent areas developed at the bow and two zones of high WSS/TKE converging downstream of the hull, roughly parallel to flow.

4.5 Hull at 45° to flow

Figure 6 shows typical CFD simulations for the submerged hull at an incident angle of 45° under a uni-directional flow of velocity 1.3 m s^{-1}. At 45°, the rotating vortex originating at the bow of the vessel dominates the 2D and 3D flow line simulations (Figures 6a and 6b). The vortex originating at the stern is negligible (Figure 6b), although still present. High velocity (Figure 6c) and high pressure (Figure 6d) zones develop in the lee of the hull, with low velocity and low pressure zones at their edges. Strong correlation between the WSS (Figure 6e) and TKE (Figure 6f) plots are evident, with amplification of both in flow-parallel zones in the lee of the hull. Both zones are bordered by narrow bands of low WSS and low TKE.

4.6 Hull at 30° to flow

Figure 7 shows typical CFD simulations for the submerged hull at an incident angle of 30° under a uni-directional flow of velocity 1.3 m s^{-1}. At 30°, the rotating vortex originating at the bow of the vessel again dominates (Figures 7a and 7b), with the ensuing more open vortex aligned at 30°, parallel to the approaching flow. High velocity (Figure 7c) and high pressure (Figure 7d) zones develop in the lee of the hull, again with low velocity and low pressure zones at their edges. Strong correlation between the WSS (Figure 7e) and TKE (Figure 7f) plots are once more evident, with amplification of both in flow-parallel zones in the lee of the hull. Both zones are bordered by narrow bands of low WSS and low TKE, almost symmetrical in nature about a flow-parallel plane. Zones of high WSS and TKE are also evident at the front and originating from the bow of the hull.

4.7 Hull at 15° to flow

Figure 8 shows typical CFD simulations for the submerged hull at an incident angle of 15° under a uni-directional flow of velocity 1.3 m s^{-1}. At 15°, with the elongate hull structure

298 aligned almost parallel to approaching flow, a single tight rotating vortex originates from the
299 vessel (Figures 8a and 8b), parallel to flow. A high velocity (Figure 8c) zone extends
300 downstream from the structure, accompanied by a low velocity zone below it. High and low
301 pressure zones are developed at the front and back of the bow section respectively (Figure
302 8d). Strong correlation between the WSS (Figure 8e) and TKE (Figure 8f) plots are again
303 evident, with amplification of both in flow-parallel zones in the lee of the hull. Both zones are
304 bordered at the bottom by narrow bands of low WSS and low TKE. Zones of high WSS and
305 TKE are also evident at below the hull.
306
307 4.8 Hull at 0° to flow
308
309 Figure 9 shows typical CFD simulations for the submerged hull at an incident angle of 0°
310 under a uni-directional flow of velocity 1.3 m s^{-1}. At 0°, with the hull aligned parallel to the
311 approaching flow, a single tight flow-parallel rotating vortex originates from the stern
312 (Figures 9a and 9b). A low velocity (Figure 9c) tail extends downstream from the structure.
313 High pressure zones are developed at the bow and stern (Figure 9d) and low pressure zones
314 to the port and starboard of the vessel. Finally, alternating zones of high and low WSS
315 (Figure 9e) and TKE (Figure 9f) originate at the stern, parallel to the approaching flow.
316
317 **5. Discussion**
318
319 5.1 Flow regimes
320
321 The CFD models (Figures 3-9) successfully capture the following changes in the flow regime
322 in the environment of the wreck site: flow contraction, the generation of a horseshoe
323 vortex in front of the wreck, the formation of lee-wake vortices behind the structure, and
324 increased turbulence and shear stress in the lee of the wreck site. The modelling further
325 demonstrates that horseshoe vortices control scour at the front (upstream face) of the
326 structure, but plays no role in scouring on the lee side of the structure. No horseshoe
327 vortex shedding is observed in CFD simulations. Lee-wake vortices dominate behind the
328 structure, with low pressure zones in the lee of the wreck capturing flow. The amplification
329 and reduction of wall shear stress and turbulent kinetic energy in the lee of the vessel form
330 distinctive patterns in relation to flow direction, with strongly developed areas of amplified
331 and reduced wall shear stress and turbulent kinetic energy demonstrating good spatial
332 correlation with each other.
333
334 5.2 Erosional and depositional patterns: models outputs and model validation

When the outputs of the CFD models are compared to existing wreck scour classification schemes derived from real-world data (Caston, 1979; Quinn, 2006) and laboratory experiments (Saunders, 2005; Testik et al., 2005), strong correlation is observed between the morphology and orientation of elevated wall shear stress (WSS) and turbulent kinetic energy (TKE) in the CFD models and the location of scour features in the scour classifications. The spatial correlation between zones of elevated TKE and scour is most notable. Figure 10 shows the interpreted relationship between the erosional and depositional patterns formed in the wake of the wreck as a function of orientation to peak tidal flow derived from the CFD modelling. Scour patterns in the classification are mapped from zones of elevated TKE, and depositional patterns are mapped from zones of reduced TKE. The CFD modelling and interpretation is validated by comparison with multibeam echosounder derived elevation models of real world wreck sites (Plets et al. 2011) collected off the south coast of England (Figure 11a) and the north east coast of Ireland (Figure 11b). Both of these study sites are characterized by non-cohesive sandy seafloors and bi-directional current regimes, analogous to the CFD model environment.

For wrecks lying at 90° to flow, the CFD model predicts twin symmetrical wake scours extending downstream and local scour developed around the bow and stern of the vessel (Figure 11), with an area of deposition (thicker sediment) between the two wake scour features. When compared to real-world wreck sites (A and B in Figure 11a), the correlation between the modelled and real world environments is convincing. The more complex arrangement of erosion and deposition imaged at site B is due to the fact that the wreck is broken in two around midhips, presenting a more complex obstacle to flow.

At an orientation of 75°, the CFD model predicts two asymmetric wake scours and the development of local scour features at the bow and stern, with higher TKE values (deeper and steeper scour) at the bow, facing into the flow. Areas of deposition are predicted on the outside of the wake scours, parallel to peak flow, and immediately in the lee of the vessel, where TKE and shear stress levels are reduced (Figures 4 and 10).

At an orientation of 60°, the initially separate twin scour hollows converge into one with distance from the vessel (Figure 10). Local scour is developed at the bow and stern, with a deeper and more extensive scour feature developed around the bow, facing the incoming flow. Zones of deposition are located in the immediate lee of the vessel and as two slightly asymmetric ridges extending parallel to the main wake scour.

At an orientation of 45°, a single broad wake scour feature is interpreted, with local scour developed at the bow. Two asymmetric depositional areas are predicted along the edges of the wake scour, parallel to peak flow, with the depositional tail from the stern (the end facing away from flow) longer and broader than the tail from the bow end. When compared to a similar real-world wreck site (F in Figure 11b), the correlation between the predicted patterns and actual patterns is again compelling. Of particular note in this flow scenario is that the highly elevated TKE area in the immediate lee of the vessel (Figure 6) correlate with the steep-sided local scour pits developed on the lee sides of the wreck in response to flood and ebb tides (Figure 11b).

At an orientation of 30°, the single broad wake scour developed in the lee of the vessel is bounded by two asymmetric depositional tails, with the tail from the stern side of the vessel more extending the full length of the scour. When compared to an analogous real-world wreck site (E in Figure 11b), the correlation is once again striking. The depositional tails developed at this wreck site are up to 1 km long, with local scour developed around the bow of the structure.

At an orientation of 15°, the single lee wake scour feature dominates with the asymmetry of the depositional tails increasing further (Figure 10 and Site D in Figure 11a). At an orientation of 0°, the signatures of scour and deposition are much weaker, due to the streamlined nature of the vessel lying parallel to peak tidal flow.

The processes and patterns inferred from the CFD modelling are in broad agreement with previous studies (Caston 1979; Quinn, 2006; Saunders, 2005; Testik et al., 2005). However, the level of detail generated from the CFD modelling is much greater, and the control environment offered by the numerical modelling allows much greater understanding of linked processes and patterns.

An additional minor point of note is that the asymmetry of the modelled shipwreck (streamlined bow and square stern section) leads to slight asymmetry of scour features, particularly in the local scour pits. This result indicates the morphology of the hull of the wreck can impart a significant influence on the morphology (shape, depth etc.) of the scour and depositional features. To date, physical laboratory experiments investigating scour around fully submerged obstacles (e.g. Saunders, 2005; Testik et al. 2005) employed symmetrically shaped objects, resulting in symmetrical scour patterns.

5.3 Archaeological implications

The archaeological implications of this method are significant in that CFD allows us to examine hydrodynamic processes in detail, and make strong links between coupled hydrodynamic and sediment dynamic processes and patterns. The results therefore represent a significant breakthrough in understanding fluid flow and erosional and depositional processes and patterns at submerged wreck sites. Research into processes that form the submerged archaeological record informs effective *in-situ* conservation and preservation of archaeological sites. Understanding N-transforms at fully submerged sites in detail – specifically, the linked physical processes operating in the water column (hydro-dynamics) and on the sea floor (sediment-dynamics) - can contribute greatly to the effective *in-situ* conservation of wreck sites.

Regular site inspections are an integral part of the overall management strategy for submerged sites (MacLeod and Richards, 2011). Increasingly, baseline morphological surveys of submerged shipwreck sites employ multibeam echosounders (Plets et al., 2011), with further inspections at (ir)regular intervals to assess change in site integrity (Manders, 2009; Quinn and Boland, 2010; Bates et al., 2011; Astley et al., 2014). Over time, this can lead to sophisticated models of erosion and deposition (Manders, 2009; Astley et al., 2014; Brennan et al., 2016), albeit at a very high financial cost. Another drawback is that these approaches only allow the patterns of erosion and deposition to be investigated, with causative processes only inferred from the results.

Conversely, CFD modelling allows us to examine both patterns *and* processes, and allows us to use high-resolution multibeam echosounder data as model inputs (Smyth and Quinn, 2014). CFD modelling is relatively inexpensive, can make use of open-source software (e.g. OpenFOAM), and allows control of the modelling environment, scenario setting, and even hypotheses testing. This approach is required to broaden our understanding of the processes impacting submerged wreck sites, to inform policy makers, and to develop effective mitigation strategies to minimise loss in the face of increasing human (e.g. offshore developments) and natural (e.g. increased storminess associated with climate change) forcing.

Due to the vast number of wrecks discovered on and under the seabed, and the prohibitive costs involved in excavating, raising and conserving these structures, the past two decades has seen a move toward *in-situ* preservation; to protect, monitor, and manage underwater archaeological sites where they lie on the seabed (Gregory et al., 2012). This approach is encouraed in the 2001 UNESCO Convention for the Protection of the Underwater Cultural

446 Heritage (UNESCO, 2001), which advises that underwater cultural heritage should be
447 protected *in-situ* as a first option and non-intrusive methods to document and study these
448 sites *in-situ* should be used (Gregory et al., 2012). The CFD approach used in this study
449 makes important contributions to not only understanding the processes acting on
450 shipwrecks, but also highlights areas where *in-situ* preservation measures could be
451 concentrated and targeted (in areas of high turbulence and shear stress), and therefore
452 allows the development of sophisticated plans for *in-situ* preservation.
453
454 **Acknowledgements**
455
456 The MBES data presented in Figure 11a contains public sector information, licensed under
457 the Open Government License v2.0, from Fugro EMU. The MBES data presented in Figure
458 11b contains public sector information, licensed under the Open Government License v2.0,
459 from the Royal Navy. All numerical modelling, data processing and data rendering in this
460 study was conducted in open source software; we acknowledge the OpenFOAM, Paraview,
461 QGIS and Inkscape community and developers. Thanks to Craig Dyer (Fugro EMU) for
462 useful discussion and for pointing us in the direction of the MBES data off Dartmouth.
463 Reviews by two anonymous reviewers greatly improved an earlier version of this
464 manuscript.
465
466
467 **References**
468
469 Arnold, J.B., Oertling, T.J., Hall, A.W., 1999. The Denbigh Project: initial observations on a
470 Civil War blockade-runner and its wreck-site. Int. J. Naut. Archaeol. 28, 126-144.
471
472 Astley, A., Dix, J.K., Thompson, C., Sturt, F., 2014. A seventeen year, near-annual,
473 bathymetric time-series of a marine structure (SS Richard Montgomery). In: Cheng, L.,
474 Draper, S. and An, H. (Eds.), Scour and Erosion: Proceedings of the 7th International
475 Conference on Scour and Erosion. International Conference on Scour and Erosion. Taylor &
476 Francis, pp 715-724.
477
478 Baeye, M., Quinn, R., Deleu, S., Fettweis, M., 2016. Detection of shipwrecks in ocean colour
479 satellite imagery. J. Archaeol. Sci. 66, 1-6.
480
481 Ballard, R.D., McCann, A.M., Yoeger, D., Whitcomb, L., Mindell, D., Oleson, J., Singh, H.,
482 Foley, B., Adams, J., Piechota, D., Giangrande, C., 2000. The discovery of ancient history in

the deep sea using advanced deep submergence technology. Deep-Sea Res. Pt I. 47: 1519-1620.

Ballard, R.D., Stager, L.E., Master, D., Yoerger, D., Mindell, D., Whitcomb, L.L., Singh, H. and Piechota, D., 2002. Iron Age Shipwrecks in Deep Water off Ashkelon, Israel. Am. J. Archaeol. 106, 151-168.

Bates, C.R., Lawrence, M., Dean, M., Robertson, P., 2011. Geophysical Methods for Wreck-Site Monitoring: the Rapid Archaeological Site Surveying and Evaluation (RASSE) programme. Int. J. Naut. Archaeol. 40, 404-416.

Brennan, M.L., Davis, D., Ballard, R.D., Trembanis, A.C., Vaughan, V.I., Krumholz, J.S., Delgado, J.P., Roman, C.N., Smart, C., Bell, K.L.C., Duman, M., DuVal, C., 2016. Quantification of bottom trawl fishing damage to ancient shipwreck sites. Mar. Geol. 371, 82-88.

Caston, G.F., 1979. Wreck marks: indicators of net sand transport. Mar. Geol. 33, 193-204.

Gregory, D., Jensen, P., Strætkvern, K., 2012. Conservation and in situ preservation of wooden shipwrecks from marine environments. J. Cult. Herit. 13, S139–S148.

Hatton, K.A., Smith, H.D. and Foster, D.L., 2004. The Scour and Burial of Submerged Mines, Eos Trans. AGU. 84 (52). Ocean Sci. Meet. Suppl. Abstract OS52B-18.

Hesp, P.A., Smyth, T.A.G., Nielsen, P., Walker, I.J., Bauer, B.O., Davidson-Arnott, R., 2015. Flow deflection over a foredune. Geomorphology. 230, 64-74.

Manders, M., 2009. Multibeam recording as a way to monitor shipwreck sites. In: MACHU Final Report NR. 3 - Managing Cultural Heritage Underwater, pp. 59–66.

MacLeod, I.D., Richards, V.L., 2011. In situ conservation surveys of iron shipwrecks in Chuuk Lagoon and the impact of human intervention. AICCM Bull. 32, 106-122.

McCann, A.M. and Oleson, J.P., 2004. Deep Water Shipwrecks off Skerki Bank: The 1997 Survey. J. Roman Archaeol. Supp. Ser. 58. Portsmouth, R.I.

518 McNinch, J.E. Wells, J.T and Drake, T.G., 2001. The fate of artifacts in an energetic, shallow-
519 water environment: scour and burial at the wreck site of Queen Anne's Revenge.
520 Southeastern Geol. 40, 19-27.
521
522 Muckelroy, K., 1978. Maritime archaeology, Cambridge University Press, Cambridge.
523
524 O' Shea, J.M., 2002. The archaeology of scattered wreck-sites: formation processes and
525 shallow water archaeology in western Lake Huron. Int. J. Naut. Archaeol. 31, 211-227.
526
527 Plets, R., Quinn, R., Forsythe, W., Westley, K., Bell, T., Benetti, S., McGrath, F., Robinson, R.,
528 2011. Using Multibeam Echo-Sounder Data to Identify Shipwreck Sites: archaeological
529 assessment of the Joint Irish Bathymetric Survey data. Int. J. Naut. Archaeol. 40, 87-98.
530
531 Quinn, R., 2006. The role of scour in shipwreck site formation processes and the
532 preservation of wreck-associated scour signatures in the sedimentary record - evidence
533 from seabed and sub-surface data. . J. Archaeol. Sci. 33, 1419-1432.
534
535 Quinn, R. and Boland, D., 2010. The role of time-lapse bathymetric surveys in assessing
536 morphological change at shipwreck sites. J. Archaeol. Sci. 37, 2938-2946.
537
538 Quinn, R., Saunders, R., Plets, R., Westley, K., Dix, J., 2016. Marine scour of cohesionless
539 sediments. In: Keith, M.E. (Ed.), Site Formation Processes of Submerged Shipwrecks.
540 University Press of Florida, Gainesville, pp. 70-89.
541
542 Quinn, R., Bull, J.M., Dix, J.K and Adams, J.R., 1997. The Mary Rose site - Geophysical
543 Evidence for palaeo-scour marks. Int. J. Naut. Archaeol. 26, 3-16.
544
545 Saunders, R., 2005. Seabed scour emanating from submerged three dimensional objects;
546 archaeological case studies. Unpublished PhD Thesis, University of Southampton.
547
548 Smith, H.D., Foster, D.L., Voropayev, S.I., Fernando, H.J.S., 2004. Modelling the Turbulent
549 Processes Around a 3-D Cylinder, Eos Trans. AGU 85 (47) Fall Meeting Suppl. Abstract
550 OS21B-1217.
551
552 Smyth, T.A.G., Jackson, D.W.T., Cooper, J.A.G., 2013, Three dimensional airflow patterns
553 within a coastal trough–bowl blowout during fresh breeze to hurricane force winds. Aeolian
554 Res. 9, 111-123.

Smyth, TAG, Quinn, R., 2014. The role of computational fluid dynamics in understanding shipwreck site formation processes. J. Archaeol. Sci. 45, 220-225.

Soulsby, R., 1997. Dynamics of Marine Sands, Thomas Telford Ltd, London.

Sumer, B.M., Christiansen, N. and Fredsoe, J., 1997. The horseshoe vortex and vortex shedding around a vertical wall-mounted cylinder exposed to waves, Journal of Fluid Mechanics, 332: 41-70.

Sumer, B.M., Whitehouse, R., Torum, A., 2001, Scour around coastal structures: a summary of recent research. Coast. Eng. 44, 153-190.

Stewart, D.J., 1999. Formation processes affecting submerged archaeological sites: An overview, Geoarchaeology. 14, 565-587.

Testik, F.Y., Voropayev, S.I. and Fernando, H.J.S., 2005. Flow around a short horizontal bottom cylinder under steady and oscillatory flows. Phys. Fluids. 17, 47-103.

Trembanis, A.C., McNinch, A.C., 2003. Predicting Scour and Maximum Settling Depths of Shipwrecks: A Numeric Simulation of the Fate of Queen Anne's Revenge. Proceedings of Coastal Sediments, Clearwater Beach, Florida.

Uchupi, E., Muck, M.T., Ballard, R.D., 1988. The geology of the Titanic site and vicinity, Deep-Sea Res. Pt A. 35, 1093-1110.

UNESCO, 2001. Convention on the Protection of the Underwater Cultural Heritage. http://www.unesco.org/new/en/culture/themes/underwater-cultural-heritage/2001-convention/ Accessed 13.08.2016

Voropayev, S.I., Testik, F.Y., Fernando, H.J.S., Boyer, D.L., 2003. Burial and scour around short cylinder under progressive shoaling waves. Ocean Eng. 30, 1647-1667.

Ward, I.A.K., Larcombe, P. and Veth, P., 1999. A New Process-based Model for Wreck Site Formation. J. Archaeol. Sci. 26, 561-570.

Wheeler, A., 2002. Environmental Controls on Shipwreck Preservation: The Irish Context. J. Archaeol. Sci. 29, 1149-1159.

Whitehouse, R.J.S., 1998. Scour at marine structures, Thomas Telford Ltd., London.

Whitehouse, R.J.S., Harris, J.M., Sutherland, J., Rees, J., 2010. The nature of scour development and scour protection at offshore windfarm foundations, Mar Poll Bull. 62, 73-88.

Whitehouse, R.J.S., Sutherland, J., Harris, J.M., 2011. Evaluating scour at marine gravity structures, Maritime Eng. 164 (MA4), 143-157.

Yakhot, V., Orszag, S.A., Thangam, S., Gatski, T.B., Speziale, C.G., 1992. Development of turbulence models for shear flows by a double expansion technique. Phys. Fluids A. 4, 1510-1520.

Figures

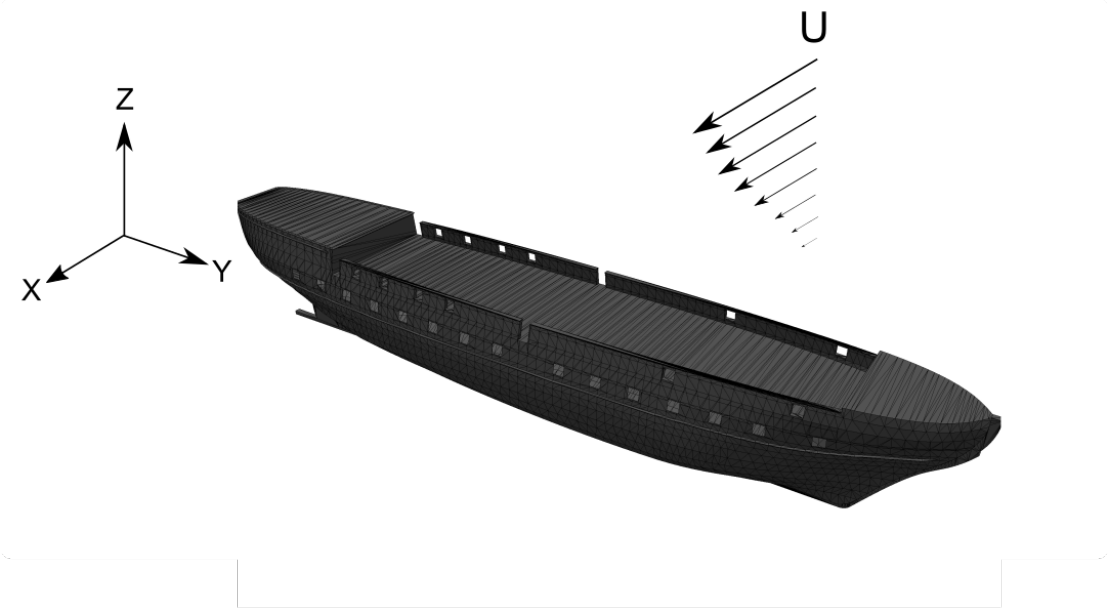

Figure 1: Illustration of the hull structure and coordinate system used in the CFD modelling. Model parameters: U = free-stream water velocity, z = height above bed, x = distance downstream of the hull model, y = distance in line with the hull orientation.

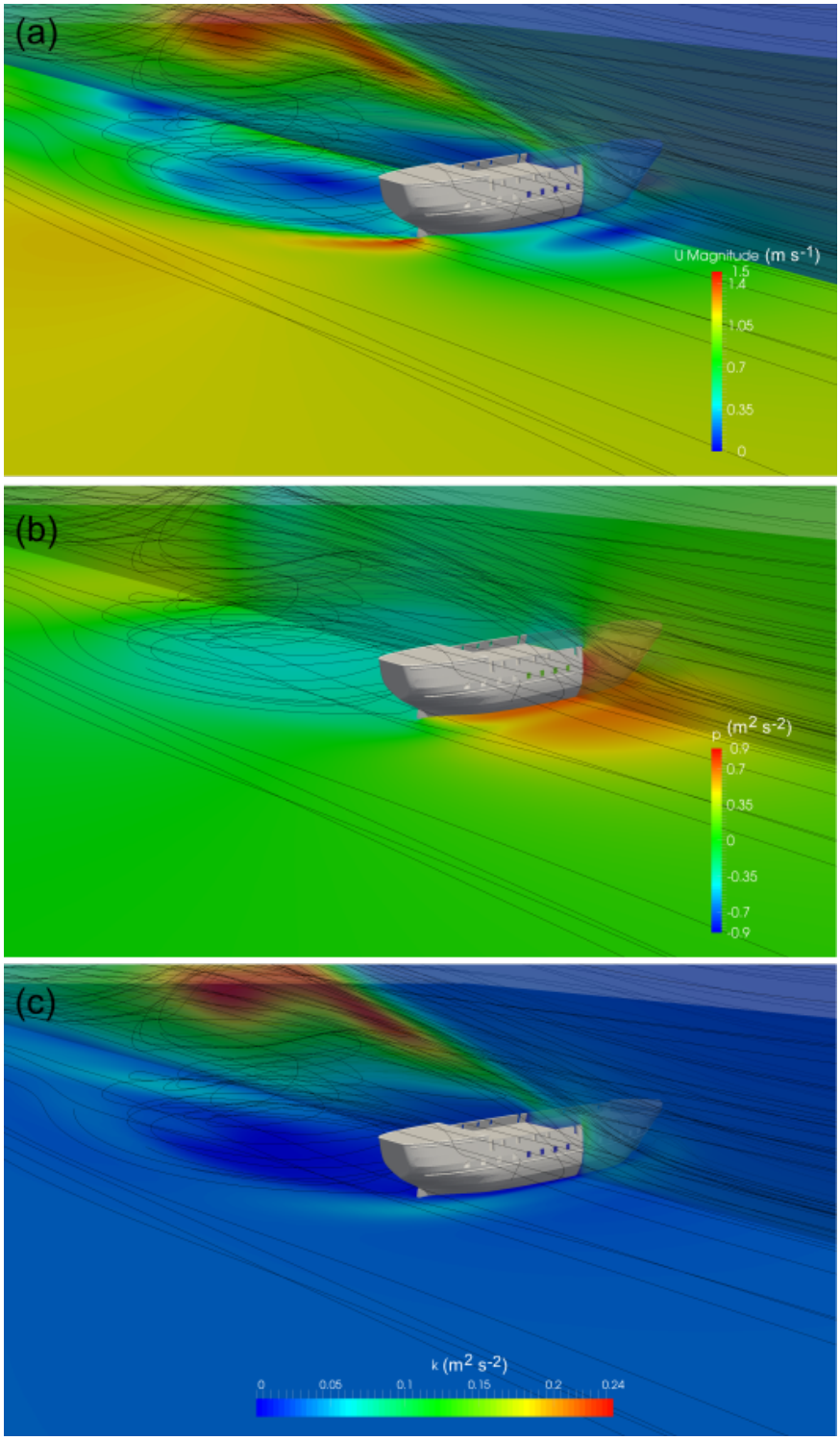

Figure 2: (a) 3D simulation with 2D vertical slice of the velocity field around the hull structure with flowlines superimposed, (b) 3D simulation with 2D vertical slice of the pressure field around the hull structure, and (c) 3D simulation with 2D vertical slice of the TKE field around the hull structure.

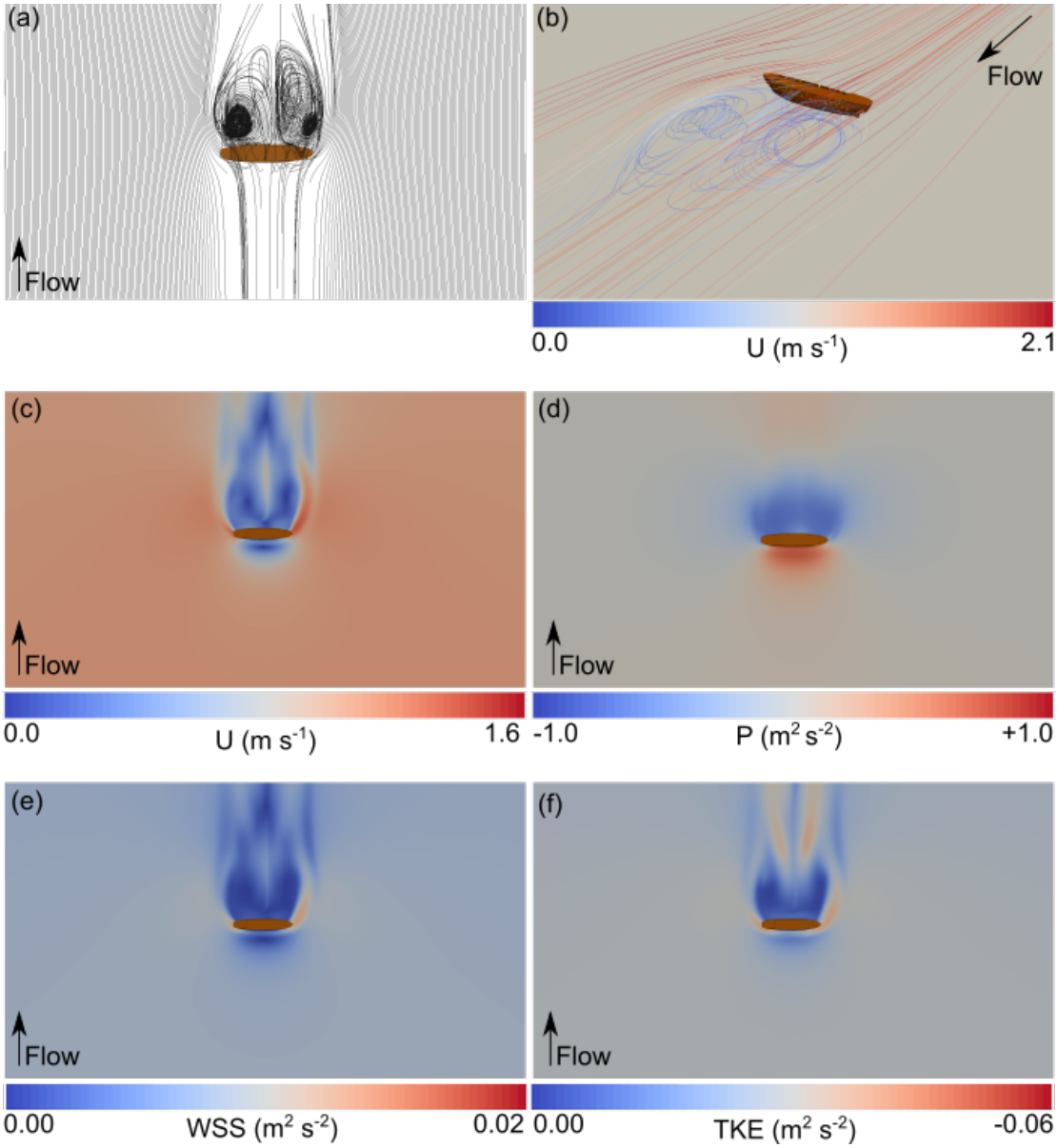

Figure 3: Hull at 90° to flow. (a) 2-dimensional flowlines, (b) 3-dimensional flowlines, (c) velocity, (d) pressure, (e) wall shear stress, and (f) turbulent kinetic energy maps derived from CFD model.

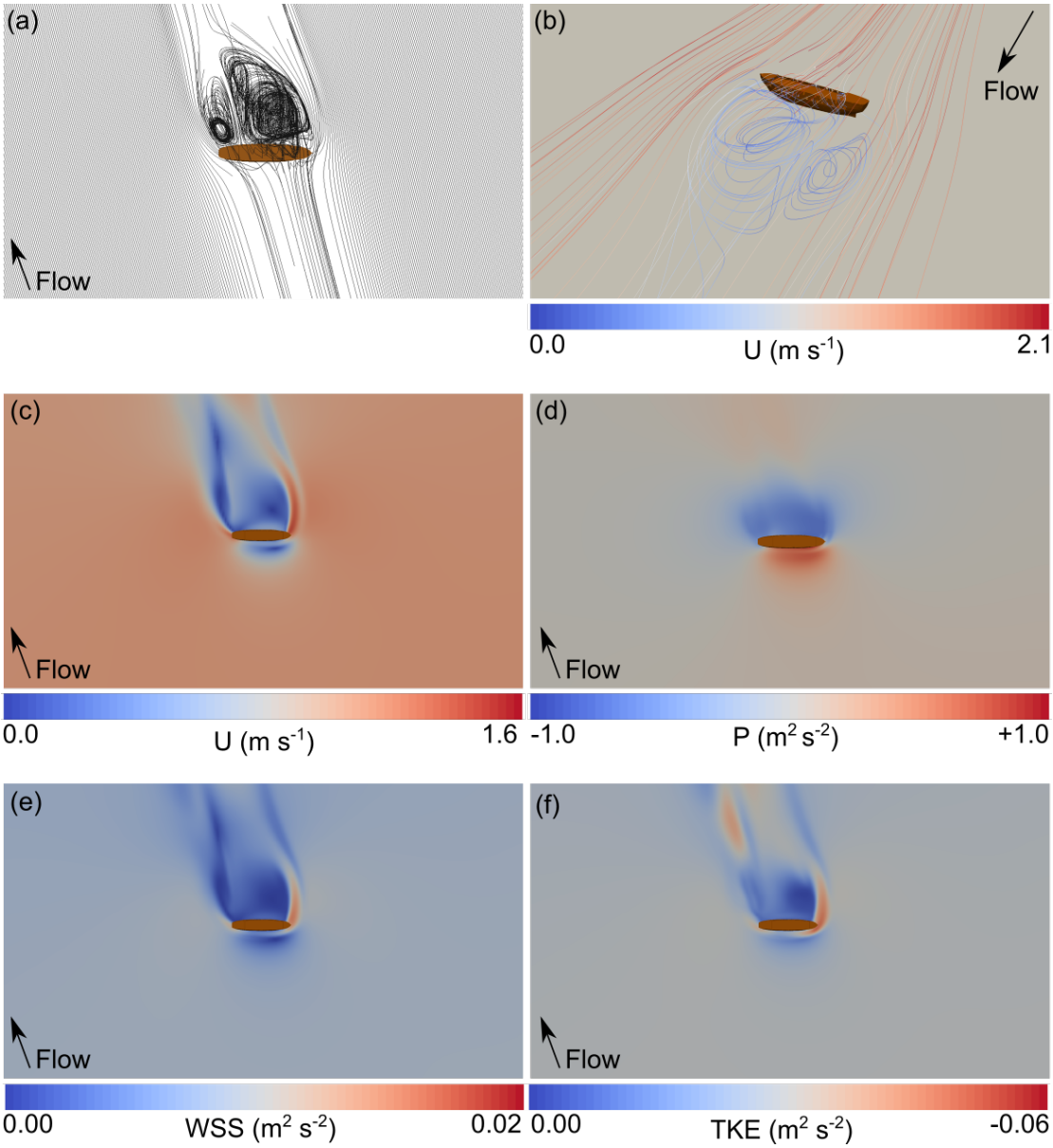

Figure 4: Hull at 75° to flow. (a) 2-dimensional flowlines, (b) 3-dimensional flowlines, (c) velocity, (d) pressure, (e) wall shear stress, and (f) turbulent kinetic energy maps derived from CFD model.

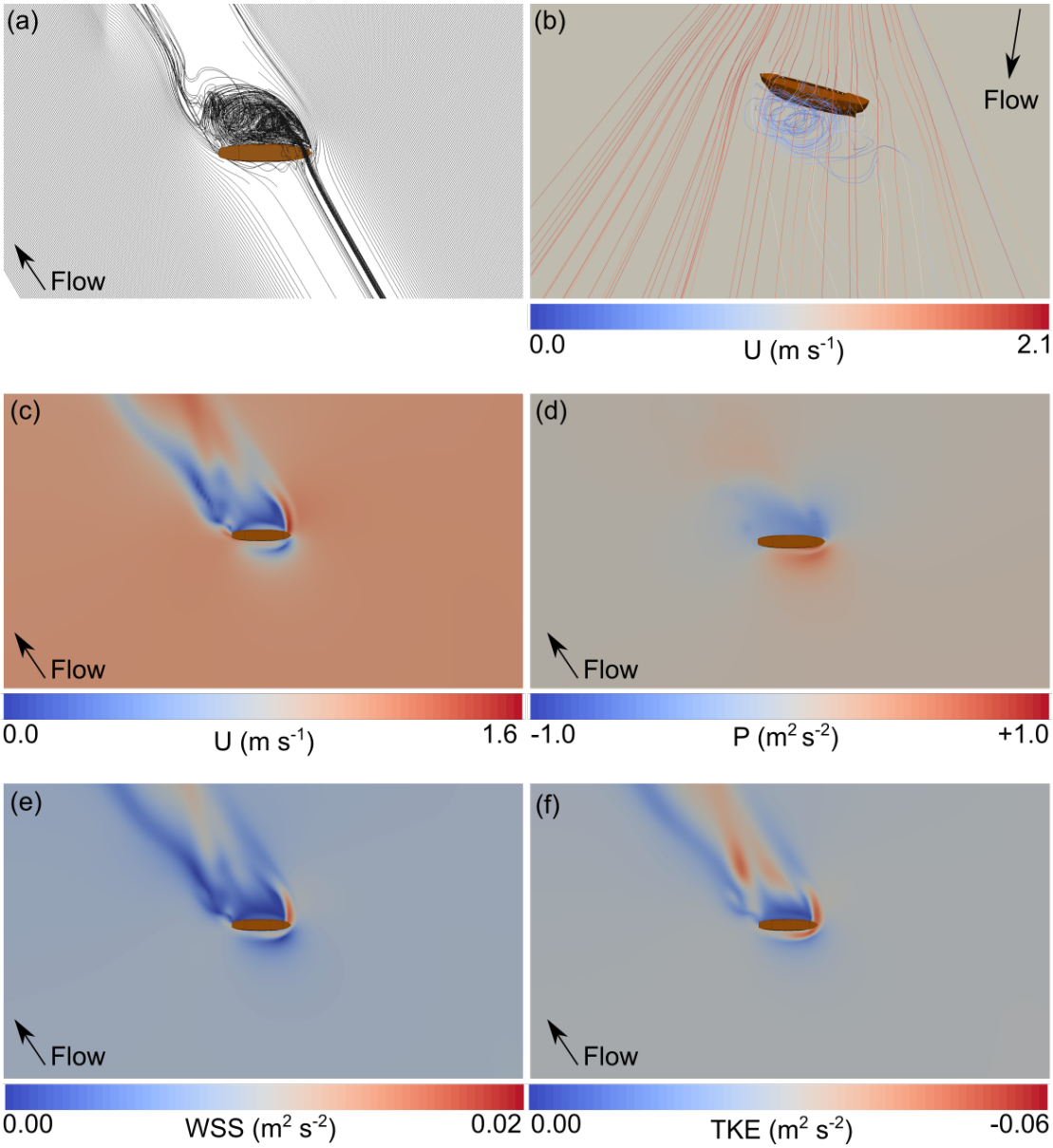

Figure 5: Hull at 60° to flow. (a) 2-dimensional flowlines, (b) 3-dimensional flowlines, (c) velocity, (d) pressure, (e) wall shear stress, and (f) turbulent kinetic energy maps derived from CFD model.

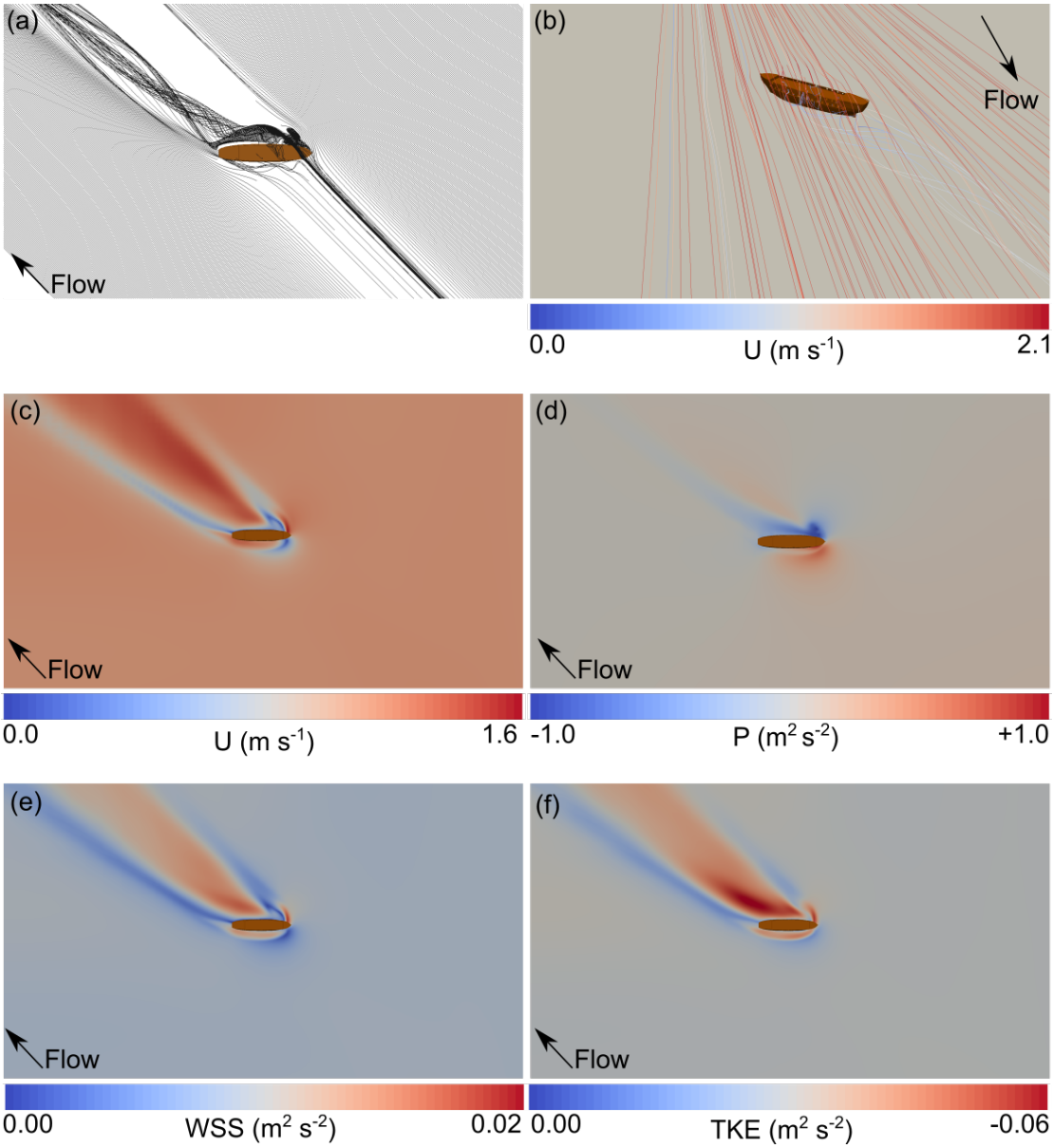

Figure 6: Hull at 45° to flow. (a) 2-dimensional flowlines, (b) 3-dimensional flowlines, (c) velocity, (d) pressure, (e) wall shear stress, and (f) turbulent kinetic energy maps derived from CFD model.

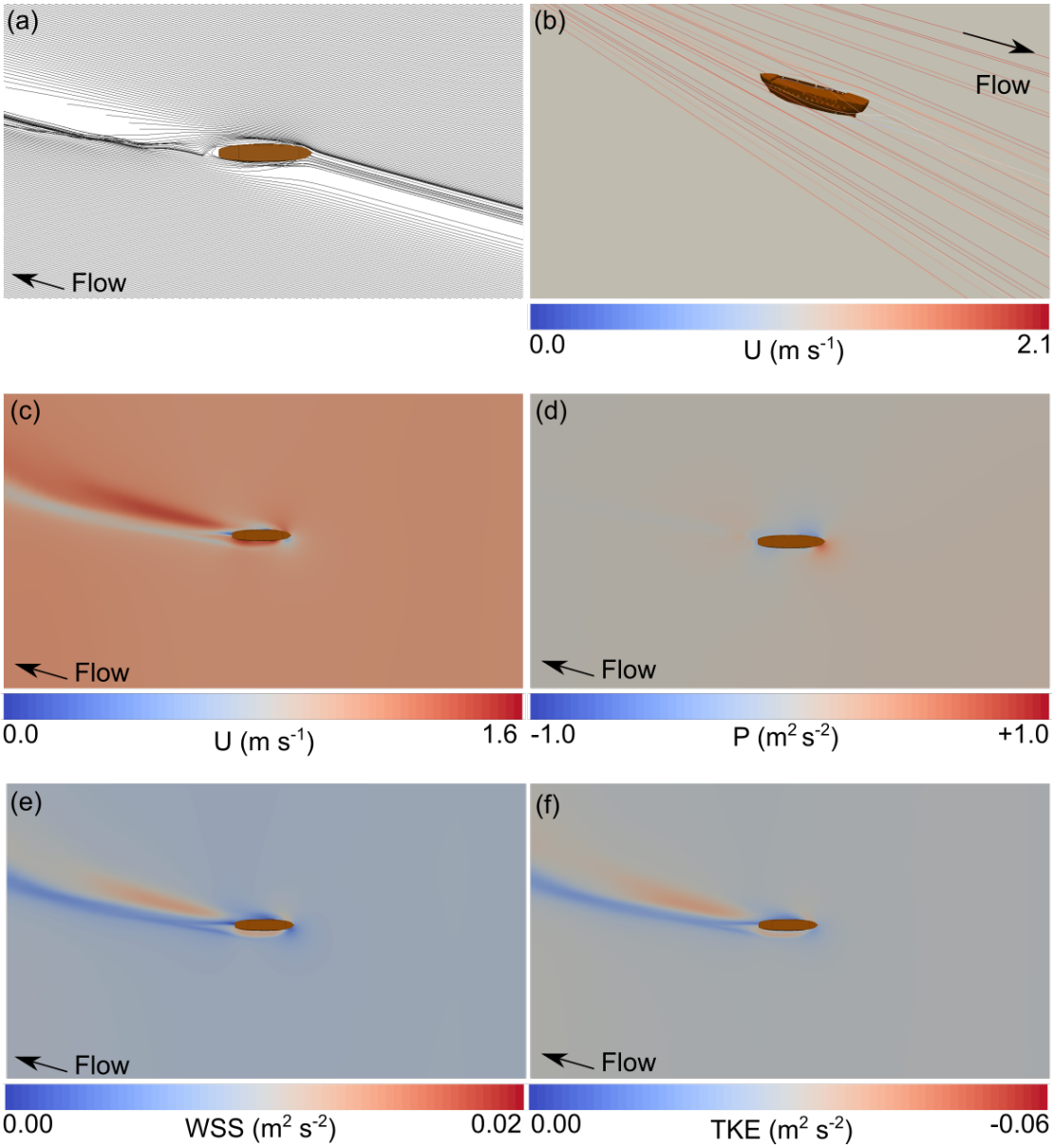

Figure 7: Hull at 30° to flow. (a) 2-dimensional flowlines, (b) 3-dimensional flowlines, (c) velocity, (d) pressure, (e) wall shear stress, and (f) turbulent kinetic energy maps derived from CFD model.

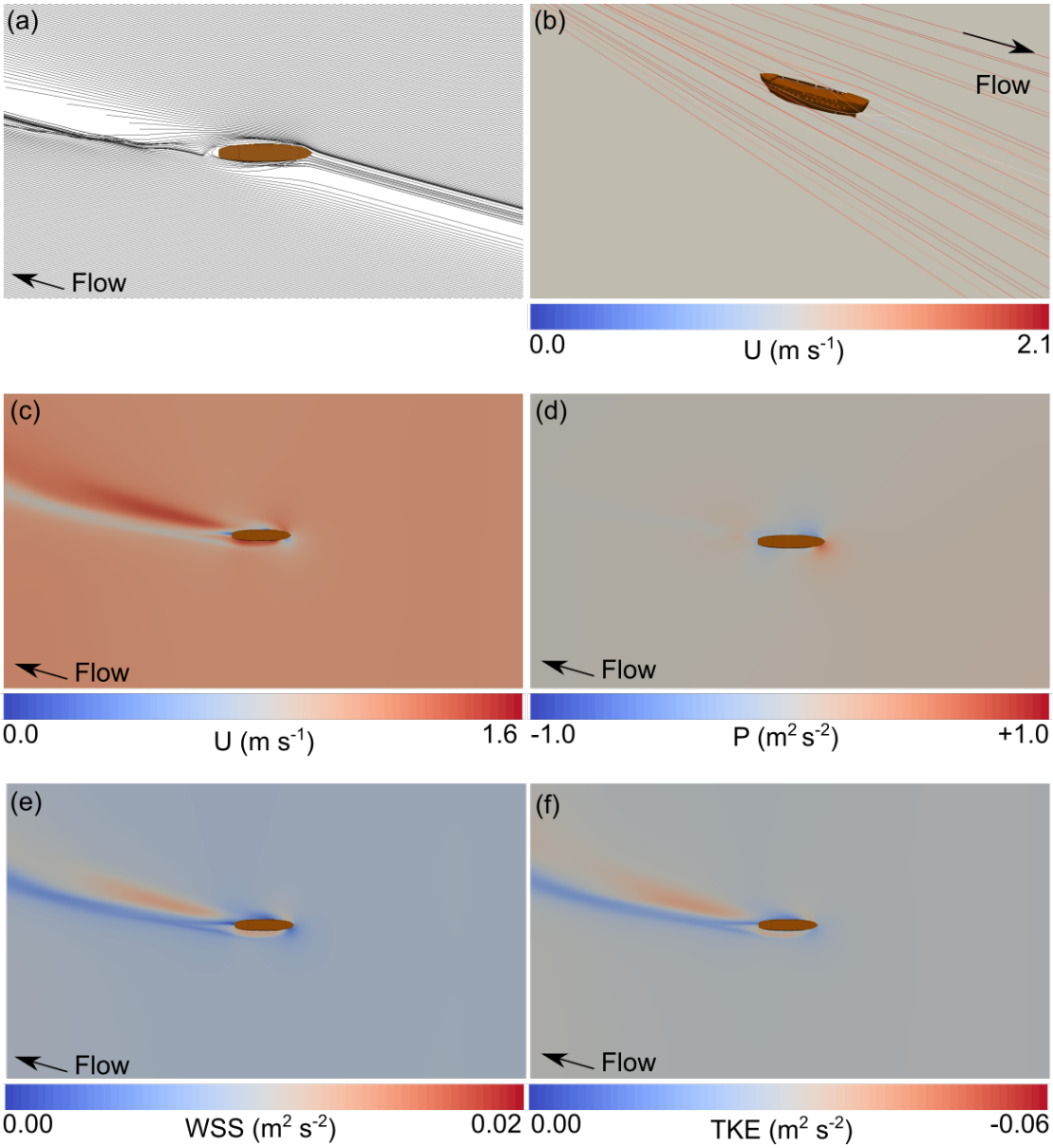

Figure 8: Hull at 15° to flow. (a) 2-dimensional flowlines, (b) 3-dimensional flowlines, (c) velocity, (d) pressure, (e) wall shear stress, and (f) turbulent kinetic energy maps derived from CFD model.

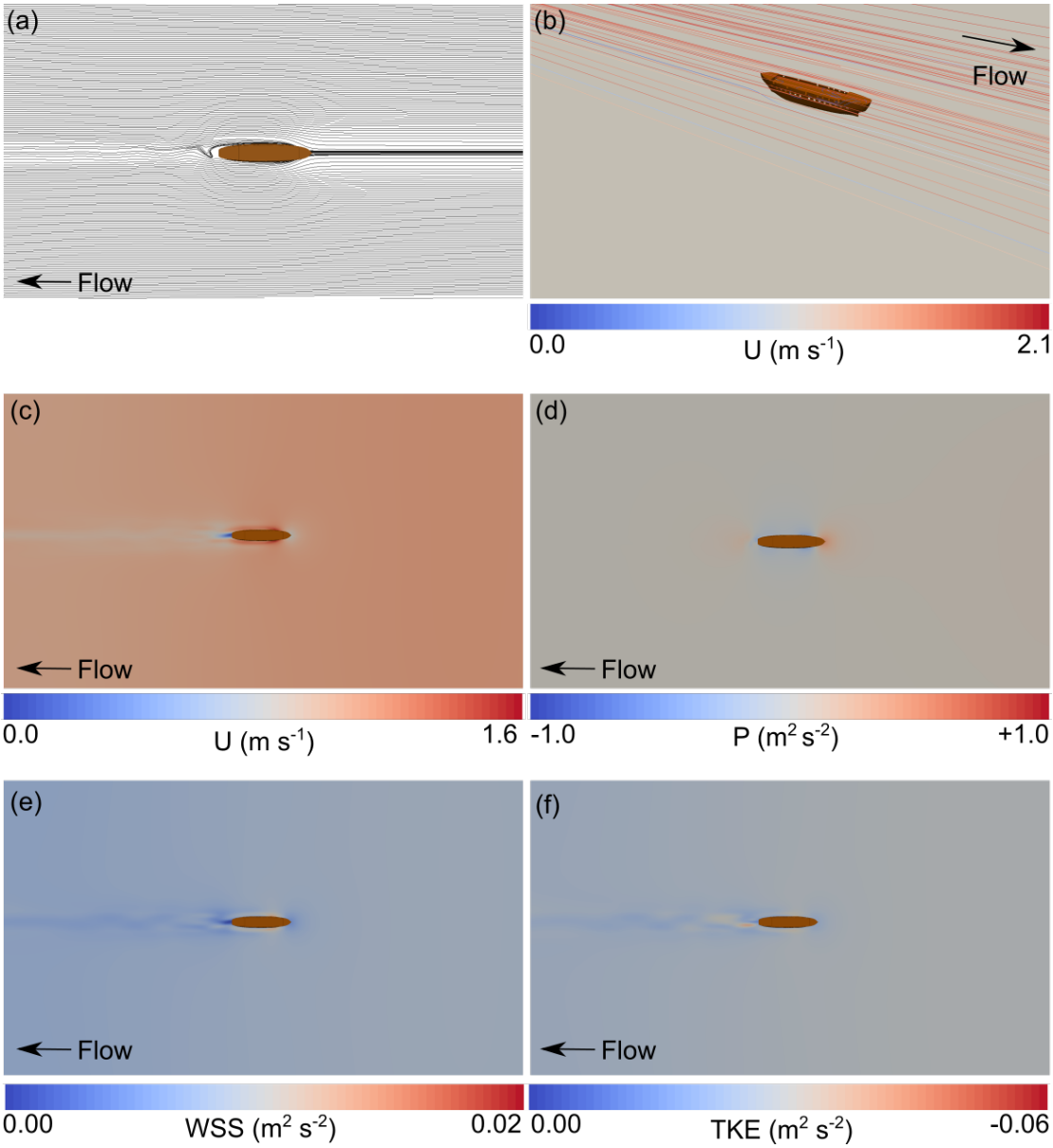

Figure 9: Hull at 0° to flow. (a) 2-dimensional flowlines, (b) 3-dimensional flowlines, (c) velocity, (d) pressure, (e) wall shear stress, and (f) turbulent kinetic energy maps derived from CFD model.

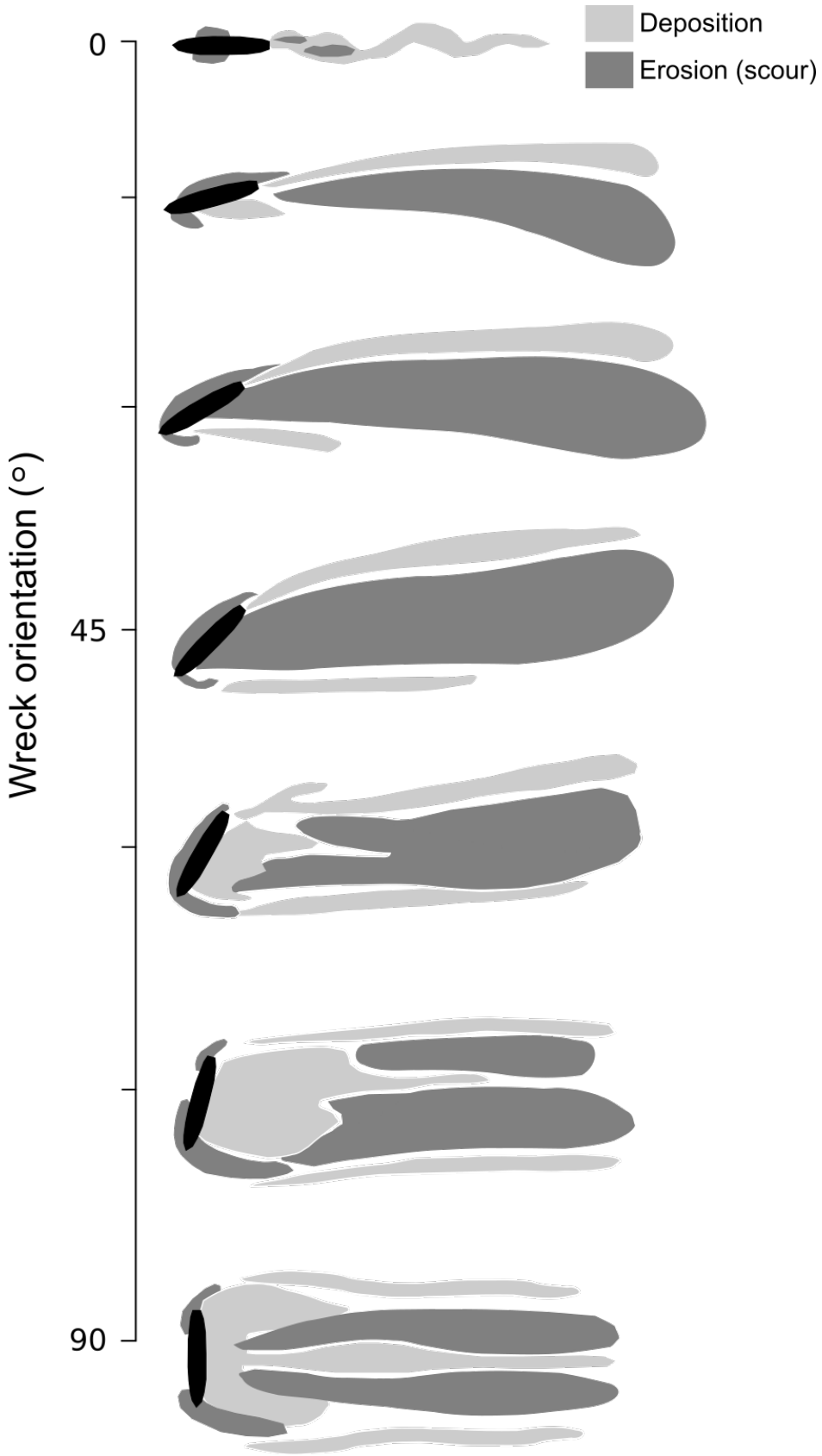

Figure 10: Wreck associated erosional and depositional patterns around fully submerged shipwrecks inferred from the output of CFD models.

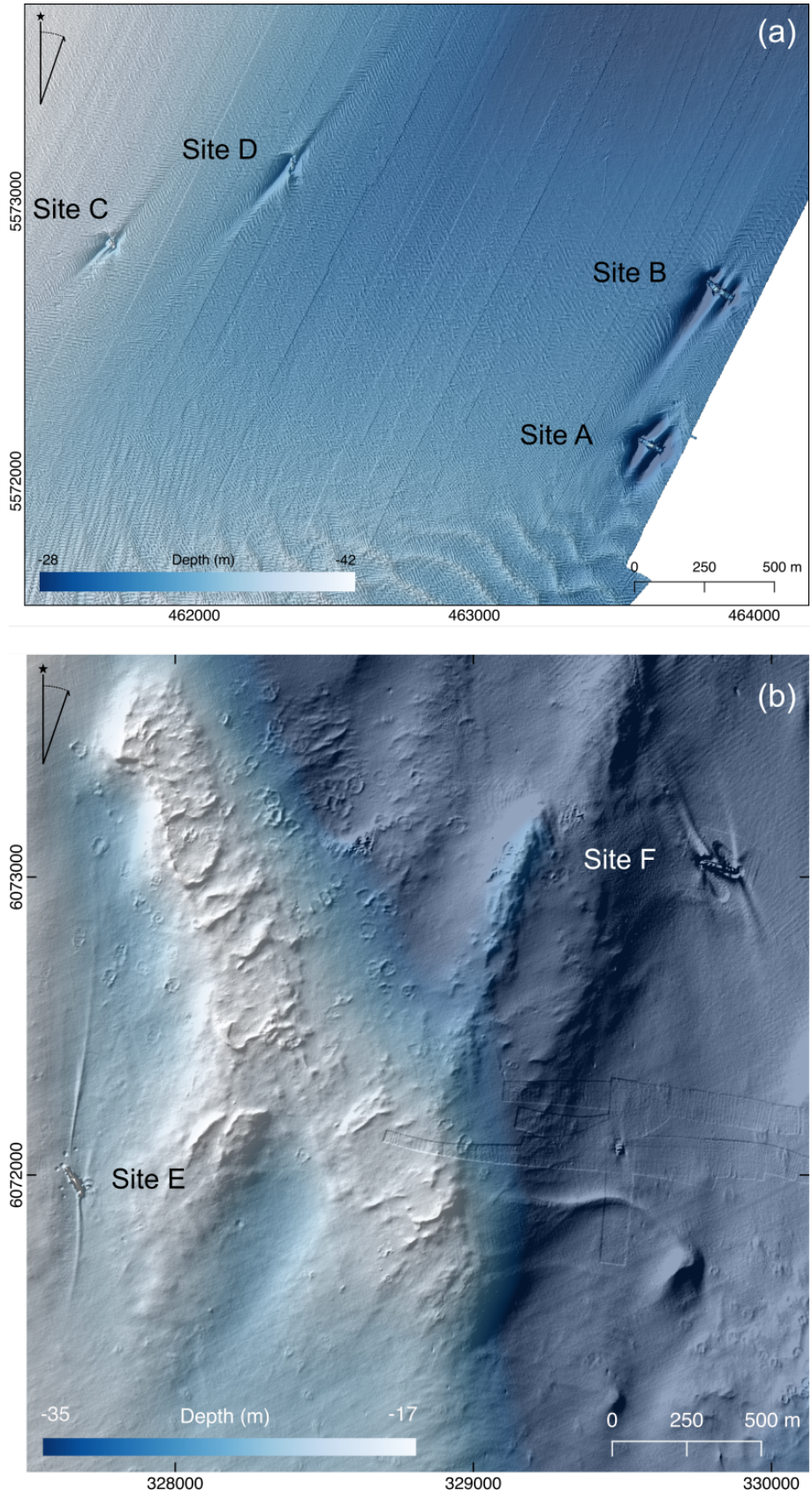

Figure 11: Multibeam echosounder data from shipwreck sites off (a) Dartmouth on the south coast of England, and (b) Belfast on the north east coast of Ireland.

670 **Table 1** Summary of flow geometry and patterns of velocity (U), pressure (P), shear stress (WSS), and turbulence (TKE) from the CFD
671 simulations.
672

Angle (°)	Flow geometry	U	P	WSS	TKE
90	Symmetrical flow patterns; horseshoe vortices form upstream; flow contraction at bow and stern; counter-rotating symmetrical low-velocity vortex pair forms downstream of wreck.	Low U zones upstream and downstream of wreck; high flow-parallel U regions originate at bow and stern.	High P zone immediately upstream of wreck; low P zone downstream.	High flow-parallel WSS regions originate at bow and stern; low WSS zones upstream and downstream of wreck.	Low TKE zones upstream and downstream of wreck; high flow-parallel TKE regions originate at bow and stern and in two symmetric diverging flow-parallel regions downstream.
75	Increasing asymmetry of flow upstream and downstream; asymmetric counter-rotating low-velocity vortex pair forms downstream; in-flow vortex dominates.	Low U zones upstream and downstream of wreck; high U region originates at upstream end; low U region originates at downstream end.	High P zone immediately upstream of wreck; low P zone downstream.	Low WSS zones upstream and downstream of wreck; high WSS region originates at upstream end; low WSS region originates at downstream end.	Low TKE zones upstream and downstream of wreck; high TKE region originates at upstream end; low TKE region originates at downstream end; two high TKE regions in wake of hull begin to converge downstream.
60	Increasing asymmetry of flow upstream and downstream; transition from asymmetric double to single vortex downstream; in-flow vortex dominates.	Low U zones upstream and downstream of wreck; high U region originates at upstream end; low U region originates at downstream end; complex U field in wake of hull.	High P zone immediately upstream of wreck; low P zone downstream elongated parallel to peak flow.	Low WSS zones upstream and downstream of wreck; high WSS region originates at upstream end; low WSS region originates at downstream end; complex WSS field in wake of hull; two high WSS regions in wake of hull converge downstream.	Low TKE zones upstream and downstream of wreck; high TKE region originates at upstream end; low TKE region originates at downstream end; complex WSS field in wake of hull; two high TKE regions in wake of hull converge downstream.
45	Single tight flow-aligned vortex forms downstream.	Single high U zone dominates in wake of hull; bounded by two low U flow-parallel regions originating at bow and stern.	High P zone immediately upstream of wreck, concentrated around upstream end; low P zone downstream elongated parallel to peak flow.	Single high WSS zone dominates in wake of hull; bounded by two low WSS flow-parallel regions originating at bow and stern.	Single high TKE zone dominates in wake of hull; bounded by two low TKE flow-parallel regions originating at bow and stern.
30	Single open flow-aligned vortex forms downstream.	Single high flow-parallel U zone dominates in wake of hull; bounded by two low U flow-parallel regions originating at bow and stern.	High P zone immediately upstream of wreck, concentrated around upstream end; paired high-low P zone downstream elongated parallel to peak flow.	Single high flow-parallel WSS zone dominates in wake of hull; bounded by two low WSS flow-parallel regions originating at bow and stern.	Single high flow-parallel TKE zone dominates in wake of hull; bounded by two low TKE flow-parallel regions originating at bow and stern.
15	Single tight flow-aligned vortex forms downstream.	Single high flow-parallel U zone dominates in wake of hull; bounded by a low U flow-parallel region originating at stern.	High P zone immediately upstream of wreck, concentrated around upstream end.	Single high flow-parallel WSS zone dominates in wake of hull; bounded by a low WSS flow-parallel region originating at stern.	Single high flow-parallel TKE zone dominates in wake of hull; bounded by a low TKE flow-parallel regions originating at

					stern.
0	Flow contraction at upstream end only; single downstream vortex forms immediately adjacent to hull.	Single flow-parallel low-velocity zone in wake of hull.	High P zone upstream and downstream of hull; low P zones at port and starboard.	Flow-parallel laterally extensive low-velocity zone in wake of hull and another at upstream end.	Flow-parallel laterally extensive low/high-velocity zone in wake of hull.